Nanoscale

PAPER

View Article Online
View Journal

Cite this: DOI: 10.1039/d5nr05160f

Morphology–phase coevolution driven by oxygen chemical potential in Fe_3O_4/α-Fe_2O_3 nanosheets

Wenkai Liu,[a] Huawei Zhao,[a] Dongqi Zhao,[a] Yupeng Zhao,[a] Muhammad Hamza Tariq,[a] Jinhong Du,[a] Ruotong Zhao,[a] Yanqing Ma *[a,b,c,d] and Lei Ma *[a,b,c]

Studies on the morphology and phase of two-dimensional (2D) non-van der Waals iron oxides are often carried out independently, leaving their coupling relationship unexplored. Herein, we report an oxygen-potential-driven chemical vapor deposition (CVD) route that couples morphology control with phase selection in the same system. We vary only the quartz-tube outer diameter to modulate the oxygen flux, which tunes the oxygen chemical potential (μ_O) without requiring any sophisticated oxygen supplying equipment and transforms the product from magnetite (Fe_3O_4) to hematite (α-Fe_2O_3). With increasing μ_O, Fe_3O_4 evolves from sharp triangular to truncated triangular nanosheets. However, regular hexagonal α-Fe_2O_3 nanosheets are obtained above this threshold, indicating morphology–phase coevolution. Opposite curvatures of Fe_3O_4 {111} A/B edges create a surface chemical-potential difference ($\Delta\mu$) that drives the evolution into nanosheets bounded solely by A-type edges. DFT calculations show that increasing μ_O reduces $\Delta\mu$, enabling the retention of the B edge and yielding truncation. Correlative magnetic imaging further reveals morphology-domain coupling: a vortex state in sharp triangles, a weakened vortex upon truncation, multidomain characteristics when approaching the hexagonal shape, and weak-ferromagnetic α-Fe_2O_3 with no magnetic phase contrast. This facile regulation method synchronizes phase selection and morphological engineering by regulating μ_O, laying the groundwork for structure-dependent spintronic device design.

Received 9th December 2025,
Accepted 26th March 2026

DOI: 10.1039/d5nr05160f

rsc.li/nanoscale

1. Introduction

Two-dimensional (2D) iron oxides, owing to high Curie temperatures with ambient stability, are an attractive material platform for spintronics.[1–3] Their redox-potentials and mixed-valence nature offer a rich compositional and phase landscape. Chemical vapor deposition (CVD) allows precise control of precursor ratios to tune the the oxygen chemical potential (μ_O). This control enables transformations among Fe_3O_4, γ-Fe_2O_3, ε-Fe_2O_3 and α-Fe_2O_3.[4] Unidirectionally aligned arrays of Fe_3O_4 nanosheets have been developed by centimeter-scale stitching using a simple and catalyst-free synthesis approach.[5] Moreover, CVD-grown α-Fe_2O_3 [6] and Fe_3O_4 [7,8] exhibit broadband photoresponses, further broadening the applications of 2D iron oxides.

CVD-grown 2D iron oxides exhibit different shapes such as triangular, truncated triangular, or hexagonal morphologies, which are commonly observed. However, this diversity and morphological tunability are often overlooked as routine phase characterization shows no clear differences. Recent work establishes a size-dependent domain configuration evolution in γ-Fe_2O_3 nanosheets. With increasing lateral size, the magnetic configuration transforms from a single domain to vortex and ultimately to multidomain patterns.[9] In addition, increasing the iron vapor pressure drives continuous morphological evolution in γ-Fe_2O_3 from triangular to stellated, petaloid, and dendritic forms.[10] Furthermore, triangular and truncated triangular Fe_3O_4 nanosheets possess different antiphase boundaries (APBs) and therefore exhibit distinct spin properties.[11] Collectively, these studies establish a consensus that 2D iron oxides offer room-temperature magnetic properties tunable by external parameters. However, despite considerable progress in understanding the morphology and phase evolution in CVD systems, their systematic coupling within a single process, together with an experimentally testable mechanism, has yet to be fully elucidated.

[a]Tianjin International Center for Nanoparticles and Nanosystems, Tianjin University, Tianjin, 300072, P. R. China. E-mail: mayanqing@tju.edu.cn, lei.ma@tju.edu.cn
[b]Tianjin Key Laboratory of Low-Dimensional Electronic Materials and Advanced Instrumentation, Tianjin, 300072, P. R. China
[c]Haihe Laboratory for Low-Dimensional Electronic Materials, Add 1 to No. 57 Wujiayao street, Hexi District, Tianjin, 300074, P. R. China
[d]School of Precision Instrument and Opto-Electronics Engineering, Tianjin University, Tianjin, 300072, P. R. China

Building on this idea, we modulate the oxygen flux by simply changing the quartz-tube outer diameter, without introducing any dedicated oxygen supplying component. This enables the tuning of μ_O, which regulates the phase transition between Fe_3O_4 and α-Fe_2O_3 within the same CVD system, while temperature, precursors, and carrier gas are held constant. Additionally, the morphology evolves continuously from sharp triangular to truncated triangular, then to near-hexagonal and finally regular hexagonal flakes. The method is simple, robust, and reproducible. At the mechanistic level, DFT combined with crystal-growth considerations shows that different curvatures of A-type and B-type edges of the {111} plane in Fe_3O_4 create a surface chemical-potential difference ($\Delta\mu$) that favors the retention of the A-type edge; as μ_O increases and $\Delta\mu$ decreases, the B-type edge becomes more stable and extends, giving rise to a truncated triangular Fe_3O_4 morphology. Upon further increase in μ_O, the truncated edge grows gradually and eventually crosses the phase transition μ_O threshold, leading to the formation of a stable hexagonal structure of α-Fe_2O_3. At the material level, the initial single-vortex magnetic domain in Fe_3O_4 weakens and shifts once truncation appears, and under the near-hexagonal geometric constraint it evolves into a multidomain state. As a control, α-Fe_2O_3 shows no discernible magnetic force microscopy (MFM) phase contrast at room temperature, underscoring the tunability of magnetic domains in iron-oxide nanosheets.

2. Experimental section

2.1 Sample preparation

Large-area, compositionally uniform arrays of 2D magnetite (Fe_3O_4) and hematite (α-Fe_2O_3) nanosheets were synthesized on mica by CVD. The growth setup is shown in Fig. S1. A square alumina crucible was filled with anhydrous $FeCl_2$ precursor (20 mg, Aladdin, ≥99.5%) and covered with a layer of 4 A molecular sieves (Thermo Fisher Scientific, 0.02–0.03 in) to slow down the $FeCl_2$ evaporation and suppress side reactions.[12,13] A freshly cleaved fluorophlogopite mica substrate (10 × 10 × 0.2 mm, Changchun Taiyuan Mica Company Ltd) was placed face-downwards about 5 mm above the precursor, and the crucible was positioned at the center of the tube furnace hot zone. 100 sccm Ar served as the carrier gas to maintain an inert atmosphere. Upon reaching the growth temperature (750 °C), the inlet flange was slightly loosened so that ambient air naturally co-flowed with Ar, thereby introducing O_2 to oxidize the Fe source on the substrate. To increase the oxygen flux per unit time, we simply switched the CVD quartz tube outer diameter from 50 mm to 60 mm, while keeping the temperature, precursor, and carrier gas unchanged. This change in the tube-diameter alters μ_O and switches the product from Fe_3O_4 to α-Fe_2O_3 without requiring any precision in the oxygen dose or additional equipment, underscoring the simplicity, robustness, and reproducibility of the method.

2.2 Characterization of iron oxides

Morphology was characterized by optical microscopy (WYJ-40BD) and non-contact atomic force microscopy (Park NX10). Magnetic domain structures were imaged on the same platform using MFM equipped with a Multi75M-G probe (Co–Cr coating, tip radius < 60 nm, coercivity ~300 Oe, effective magnetic moment ~10^{-13} emu), utilizing a lift height of 50 nm and a drive amplitude of 1 V. The Raman spectrum of the iron oxides was obtained using a confocal Raman spectrometer (532 nm excitation, 100× objective, 1 mW laser power). X-ray photoelectron spectroscopy (XPS) analysis was carried out using the PerkinElmer PHI 5100 with an Al Kα source. The crystal structure and lattice parameters were analyzed by transmission electron microscopy (JEOL JEM-F200).

3. Results and discussion

3.1 Fe_3O_4 phase synthesis and characterization

Optical microscopy (OM) reveals large area unidirectionally aligned triangular (Fig. 1a) and truncated triangular nanosheets for the samples grown using a 50 mm diameter quartz tube (Fig. 1b). Atomic force microscopy (AFM) further shows that the nanosheets retain well-defined, smooth edges even at the thickness approaching ~100 nm or larger, consistent with their morphologies (Fig. 1c and d). X-ray photoelectron spectroscopy (XPS) performed on compositionally uniform nanosheets over large areas (Fig. 1e) exhibits characteristic Fe_3O_4 signatures. The high-resolution Fe 2p spectra show 2 peaks corresponding to $2p_{3/2}$ and $2p_{1/2}$ which can be further deconvoluted into Fe^{3+} components at ~715.11 and ~727.90 eV and Fe^{2+} components at ~713.18 and ~726.13 eV, respectively.[14] In addition to C, O and Fe peaks in the XPS survey spectra (Fig. S2a), the peak at ~293.3 eV is assigned to K 2p from the fluorophlogopite mica substrate and not relevant to the synthesized nanosheets. Previous reports suggest that a strong interfacial interaction between surface K^+ on fluorophlogopite mica and Fe_3O_4 is one of the contributing factors for the unidirectional alignment observed on this substrate.[15]

For the samples which do not possess unidirectional alignment, nanosheets exhibit diverse shapes that fall into two basic categories: triangular and truncated triangular. Shape-distribution survey from a single batch shows a sharp decrease in nanosheet count with increasing truncation length; sharp triangles and short-edge truncated triangles dominate the population (Fig. 1f), and the analyzed samples are shown in Fig. S3. After transferring the samples to Au-coated Si, we performed Raman spectroscopy. The results show that, despite the shape differences, all the spectra consistently exhibit standard Fe_3O_4 fingerprints, with four peaks at ~183.3, ~306.1, ~536.2, and ~667.5 cm^{-1}, corresponding to $T_{2g}(1)$, E_g, $T_{2g}(2)$, and A_{1g} modes,[7] respectively (Fig. 1g). Additionally, no signature peaks of α-Fe_2O_3 and no characteristic broad band of γ-Fe_2O_3 in the 350–700 cm^{-1} region were observed,[9] suggesting single-phase Fe_3O_4.

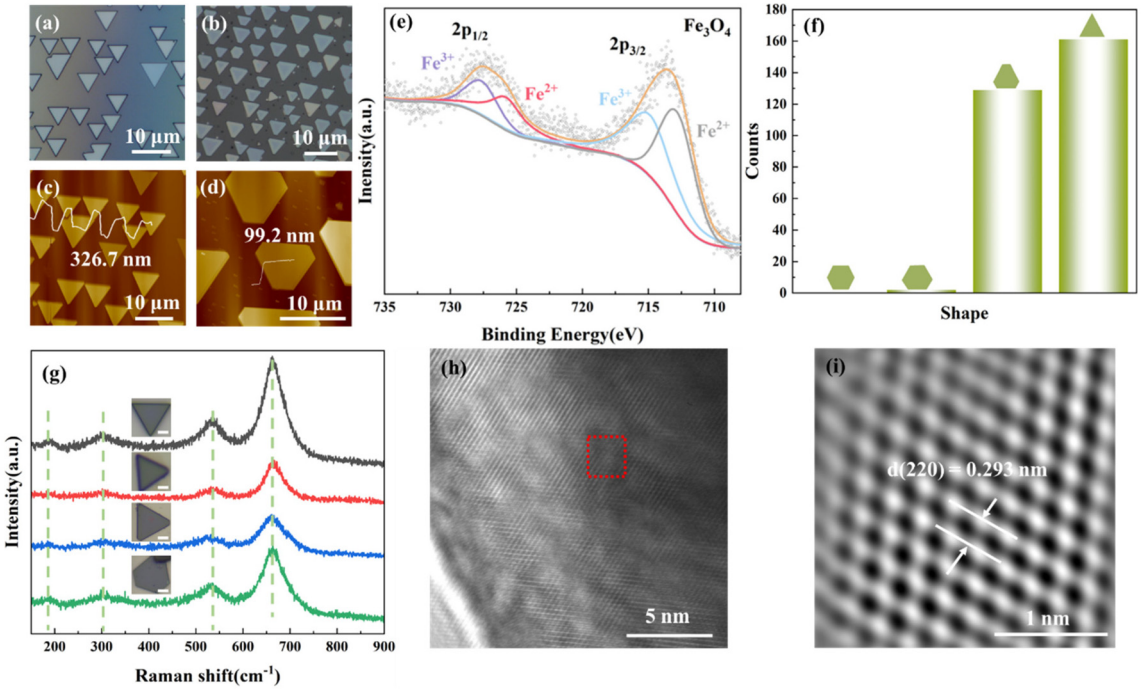

Fig. 1 Characterization of 2D Fe_3O_4 nanosheets. (a and b) Optical microscopy images of unidirectionally aligned triangular (a) and truncated triangular (b) nanosheets; (c and d) AFM images corresponding to (a) and (b), respectively; (e) high resolution XPS spectra of Fe 2p for large-area, morphology-uniform Fe_3O_4 nanosheets; (f) shape statistics for a non-aligned sample; (g) Raman spectra of Fe_3O_4 nanosheets with different morphologies; (h and i) HR-TEM lattice-structure characterization of Fe_3O_4 nanosheets. Scale bars as indicated.

Nevertheless, the different shapes are not entirely equivalent. Under 532 nm Raman excitation, sharp triangular nanosheets remain stable. At the same laser power, truncated triangular nanosheets undergo oxidation to α-Fe_2O_3 (Fig. S4). These observations indicate the metastability of truncated-triangular Fe_3O_4. This laser-induced oxidation also represents a viable route of phase transformation for iron-oxide phases.[16]

High-resolution transmission electron microscopy (HR-TEM) reveals the lattice fringes of Fe_3O_4 (Fig. 1h). In the magnified region (red box), the interplanar spacing $d \approx 0.293$ nm is indexed to the Fe_3O_4 (220) planes (Fig. 1i).[5] The lattice is well ordered without observable defects or distortions, confirming the single-crystalline nature of the nanosheets.

3.2 α-Fe_2O_3 phase synthesis and characterization

To further extend the accessible phases under the same experimental protocol, the actual intake of air (O_2) must be increased. At higher μ_O, an increased O/Fe ratio can drive the product from Fe_3O_4 toward higher oxidation states such as γ-Fe_2O_3, ε-Fe_2O_3 and α-Fe_2O_3.[4] Accordingly, we replaced the 50 mm tube with a 60 mm tube while keeping all other parameters unchanged. The increased cross-section of the air inlet allows more ambient air to flow, increasing the oxygen flux. For a given volumetric flow rate Q, average velocity $\bar{v}$ in a tube of outer diameter D satisfies the following relation:

$$\bar{v} = \frac{Q}{A} = \frac{4Q}{\pi D^2}$$

Here, A is the tube cross-sectional area and D is the tube outer diameter. Accordingly, the mean cross-sectional gas velocity satisfies $\bar{v} \propto 1/D^2$, so the 60 mm tube yields a smaller $\bar{v}$ at the same volumetric flow. In addition, the O_2 entering through the loosened inlet flange follows a steady one-dimensional convection–diffusion profile:

$$C(z) = C_0 e^{\left(-\frac{\bar{v}}{D_m} z\right)}$$

where D_m is the molecular diffusivity of O_2 in Ar, C_0 is the O_2 concentration at the inlet, and z is the distance from the inlet along the tube. According to this expression, a decrease in $\bar{v}$ increases $C(z)$, thereby increasing the O_2 concentration at the crucible position.

Hexagonal iron-oxide nanosheets were synthesized on fluorophlogopite mica (Fig. S5) and α-Al_2O_3; on α-Al_2O_3, the nanosheets exhibit strict unidirectional alignment (Fig. 2a and b). The corresponding AFM measurements confirm the alignment and reveal atomically flat surfaces (Fig. 2c and d), indicating high synthesis quality. α-Al_2O_3 and α-Fe_2O_3 both possess hexagonal lattices, leading to a strong lattice compatibility at the interface. As a result, α-Fe_2O_3 readily grows with unidirectional alignment on α-Al_2O_3 but possesses a lower degree of alignment on fluorophlogopite mica.[17,18] In a single batch (Fig. S6), hexagons overwhelmingly dominate the population (Fig. 2e). Notably, these shape statistics contrast sharply with those of Fe_3O_4 (Fig. 1f).

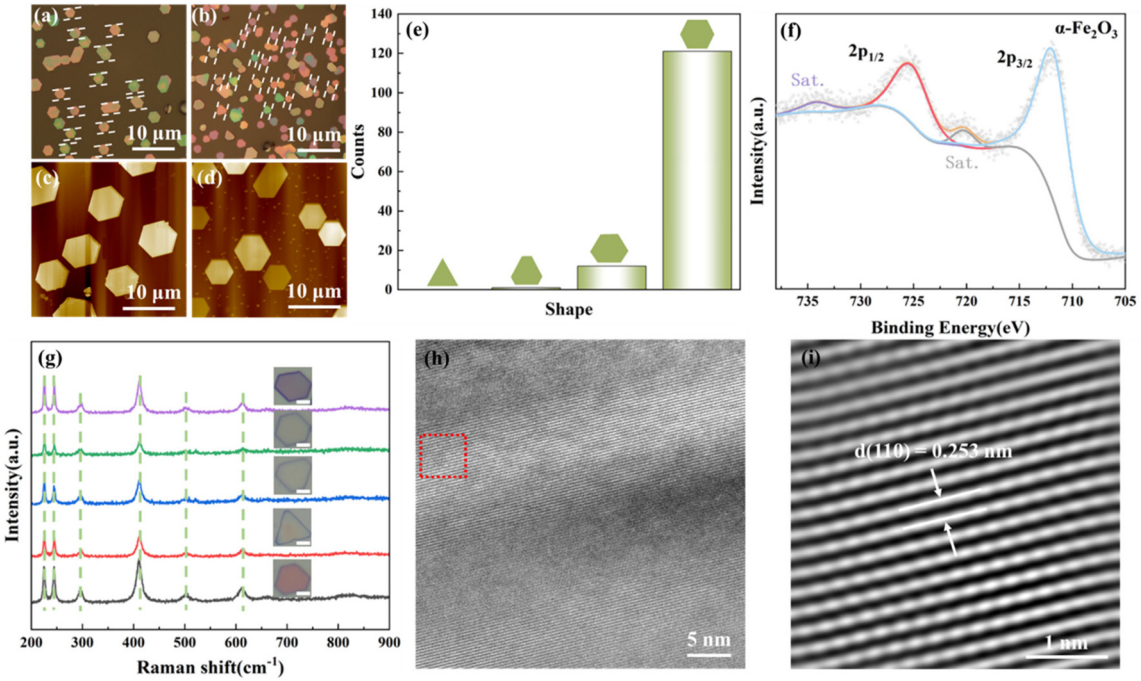

Fig. 2 Characterization of 2D α-Fe_2O_3 nanosheets. (a and b) Optical microscopy images of unidirectionally aligned hexagonal nanosheets; (c and d) AFM images corresponding to (a) and (b), respectively; (e) shape statistics for samples synthesized on α-Al_2O_3; (f) XPS results for large-area, morphologically uniform α-Fe_2O_3 nanosheets; (g) Raman spectra of α-Fe_2O_3 nanosheets with different shapes; (h and i) HR-TEM lattice-structure characterization of α-Fe_2O_3 nanosheets. Scale bars as indicated.

The high resolution XPS spectrum of Fe 2p for morphologically uniform nanosheets grown on mica shows the main Fe^{3+} peaks at ~725.11 eV ($2p_{1/2}$) and ~711.72 eV ($2p_{3/2}$) along with the distinct α-Fe_2O_3 satellite features at ~734.07 and ~720.21 eV (Fig. 2f).[19] The survey spectrum is shown in Fig. S2b. The Raman spectrum obtained for the hexagonal nanosheets of slightly different shapes is identical in peak position and line shape (Fig. 2g). The peaks at ~225.1 and ~502.5 cm^{-1} are assigned to A_{1g} modes, while those at ~244.5, ~296.4, ~410.5, and ~611.7 cm^{-1} correspond to E_g modes.[20] These peaks are well resolved, sharp, and free of shoulders, evidencing the high crystal quality. Furthermore, the Raman fingerprints of γ-Fe_2O_3 and ε-Fe_2O_3 were not observed within the detection limits.[9,21]

Consequently, increasing the tube diameter from 50 mm to 60 mm tunes the product from triangular or truncated-triangular Fe_3O_4 to hexagonal α-Fe_2O_3. In Fig. 2h, the hexagonal nanosheets show well-resolved lattice fringes; in the magnified region (Fig. 2i), an interplanar spacing of $d \approx 0.253$ nm is indexed to the α-Fe_2O_3 (110) planes, confirming the high crystal quality.

As noted above, Fe_3O_4 typically appears as triangular or truncated triangular nanosheets, whereas α-Fe_2O_3 preferentially forms regular hexagons. This variation motivates us to investigate the correlation between the oxidation state and the morphology. We propose that increasing the oxygen chemical potential (μ_O) drives a coordinated evolution of the morphology and oxidation state in 2D iron oxides: sharp triangles correspond to lower oxidation states (dominated by Fe_3O_4), while hexagons correspond to higher oxidation states (dominated by α-Fe_2O_3), whereas truncated triangles represent intermediate states.

3.3 μ_O drives shape and phase coupling calculations

In HR-TEM analysis, the triangular and truncated triangular Fe_3O_4 nanosheets show the same selected-area electron diffraction (SAED) pattern with the [111] axis (Fig. 3a and b), whereas the hexagonal α-Fe_2O_3 shows the [001] axis (Fig. 3c). The identical SAED patterns for Fe_3O_4 indicate that the morphological evolution does not arise from alteration of the crystallographic orientation; it resides at the edge terminations. To rationalize the shape evolution, we combined first-principles calculations with crystal-growth considerations.

For fcc Fe_3O_4, viewed along [111], a {111} twin plane is often present on the surface (Fig. 3d). This twin plane renders the two opposing facets inequivalent, giving a convex (A) and a concave (B) termination.[22,23] According to the Gibbs–Thomson relation in crystal growth, the chemical potential μ of the same crystallographic plane depends on local curvature k as follows

$$\mu = \mu_{flat} + \gamma_{111}\Omega k$$

Here, μ_{flat} denotes the local surface chemical potential, γ is the surface energy, Ω is the atomic volume, and k is the curvature (taken positive for convex). From the above relation, the concave B edge ($k_B < k_A$) has a lower μ than the convex A edge, so atoms attach more readily to the B edge, and its growth rate

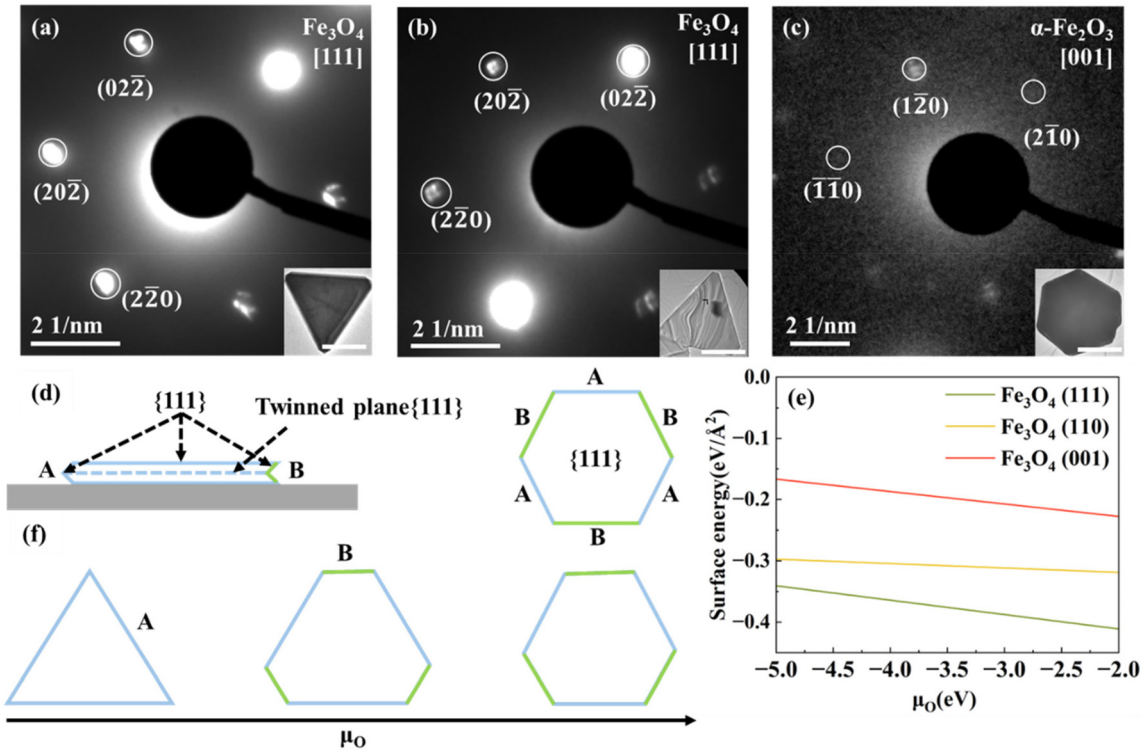

Fig. 3 Evolution of boundaries and morphology for Fe_3O_4 and α-Fe_2O_3. (a–c) SAED patterns of Fe_3O_4 nanosheets along [111] and α-Fe_2O_3 nanosheets along [001]; insets show the corresponding morphologies. Inset scale bar: 1 μm; (d) schematic of Fe_3O_4 side edges: alternating A/B edges on {111}, presenting convex (A) and concave (B) terminations; (e) first-principles surface energies of three Fe_3O_4 facets as a function of μ_O; (f) schematic of Fe_3O_4 morphology evolution; with increasing μ_O, the concave B edge is progressively retained and extended.

is higher ($V_B > V_A$). As the growth proceeds, the B edge is overgrown, and the outer contour is set by the slower A edge, yielding Fe_3O_4 triangles bounded entirely by convex A facets.

We performed first-principles calculations for the surface energy of Fe_3O_4 facets as a function of μ_O. When μ_O is below around −2.0 eV, oxidation favors Fe_3O_4 with Fe^{3+} and Fe^{2+}. Above this threshold, the product tends to be Fe_2O_3 with Fe^{3+} only.[24] The computed surface energies of Fe_3O_4 decrease with increasing μ_O (Fig. 3e), which minimizes the Gibbs–Thomson effect, reduces the growth-rate disparity between A and B edges, and passivates the boundary. With further increase in μ_O, the B edge continues to extend (Fig. 3f). Based on the Wulff construction, the emergence of these truncated edges (Type-B) signifies the exposure of facets with higher surface energy compared to the stable Fe-terminated edges (Type-A). These high-energy boundaries contain a higher concentration of under-coordinated atoms, rendering the truncated nanosheets more susceptible to external stimuli. This energetic disparity satisfactorily explains the preferential laser-induced oxidation observed in Raman studies, where the phase transformation initiates at these metastable truncated corners. Nevertheless, a residual growth-rate difference persists, making it unlikely for A and B edges to reach equal length accounting for the near absence of perfectly hexagonal Fe_3O_4 nanosheets.

By contrast, α-Fe_2O_3 viewed along [001] is bounded laterally by equivalent {110} prismatic facets without concave/convex asymmetry,[25] so the six edges are symmetrically equivalent and their sidewall growth rates are nearly identical, yielding regular hexagons. Consistent with these considerations, our experiments show a continuous shape transition from triangular Fe_3O_4 to hexagonal α-Fe_2O_3.

3.4 Influence of morphology on magnetic domains

The magnetic domain structures were imaged *in situ* using magnetic force microscopy (MFM) with a Multi75M-G probe. To strictly decouple magnetic signals from topography, the measurements were performed in interleave lift mode with a lift height of 50 nm. Comprehensive control experiments confirming the signal robustness under varying lift heights and drive amplitudes are provided in Fig. S7, definitively ruling out topographic artifacts; MFM *in situ* non-contact mode (NCM) topography reveals flat surfaces (Fig. S8), demonstrating the accuracy of our phase imaging.

Generally speaking, the domain structure of a magnetic crystal or film is dependent on its magnetic parameters (such as exchange, anisotropy and magnetization) and its geometry.[26] For most samples above a critical size, the geometry does not play a critical role, and a single-domain state is energetically unfavorable due to its high magnetostatic energy. Therefore, the sample splits into multiple magnetic domains to reduce the magnetostatic energy in the absence of an external magnetic field.[27] In contrast, when the sample is reduced

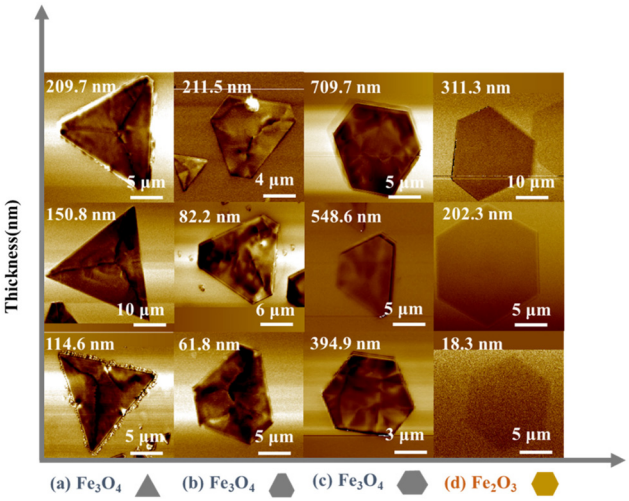

Fig. 4 MFM images of morphology-coupled 2D Fe_3O_4 and α-Fe_2O_3. MFM phase maps arranged along the horizontal axis by the morphology: (a) sharp triangular Fe_3O_4; (b) truncated triangular Fe_3O_4; (c) near-hexagonal Fe_3O_4; (d) hexagonal α-Fe_2O_3. The vertical axis lists the selected nanosheet thicknesses. Scale bars as indicated.

below a critical size, the formation of domains is geometrically confined, and the magnetic configuration is then governed by the competition among exchange, magnetostatic, and anisotropy energies. To minimize the magnetostatic energy, the magnetization should lie in the plane to avoid surface magnetic charges and align parallel to local edges to avoid edge magnetic charges.[28] This leads to the formation of a flux-closure domain, often referred to as a magnetic vortex.

As shown in Fig. 4a, sharp-triangular Fe_3O_4 nanosheets exhibit a robust single-vortex state, with domain walls extending from the central vortex core towards the three corners. In this magnetic configuration, the magnetic flux is closed in the plane to reduce the magnetostatic energy, while the magnetization in the vortex core is tilted out of plane to reduce the exchange energy, which constitutes the magnetic ground state of the triangular Fe_3O_4 nanosheets.[26,28] As the vertices are eliminated (Fig. 4b), the resulting truncated edges reduce the corner magnetic charges and create a lower-energy flux channel along the edges, which displaces the vortex and eventually makes it indistinguishable. Interestingly, this truncated triangular geometry can hold antivortex states in polycrystalline ε-Fe_2O_3,[29,30] whose large magnetocrystalline anisotropy does not hinder but facilitates stabilizing an antivortex state. In near-hexagonal Fe_3O_4 nanosheets (Fig. 4c), multiple boundaries impose stronger confinement, and a multidomain pattern, characterized by alternating bright and dark contrast, is observed. In contrast, α-Fe_2O_3 shows no observable MFM phase contrast at room temperature (Fig. 4d), consistent with its weak ferromagnetism. In addition, the thickness does not seem to be a dominant factor for the magnetic configuration in these scenarios, since our samples with the same geometry but across a wide range of thicknesses exhibit similar domain patterns. This correlation between morphology and magnetic domain paves the way for tailoring the initial magnetic properties in Fe_3O_4 through geometric engineering.

4. Conclusions

In summary, we synthesized two-dimensional Fe_3O_4 and α-Fe_2O_3 nanosheets by CVD and identified the two phases by Raman spectroscopy and XPS. With increasing μ_O, the morphology evolves from sharp-triangular Fe_3O_4 to hexagonal α-Fe_2O_3, with truncated-triangular nanosheets as an intermediate state. First-principles calculations rationalized this evolution by showing that higher μ_O reduces the growth-rate disparity between inequivalent edges, thereby weakening the curvature-driven preference and passivating the boundary. In addition, MFM reveals a difference in magnetic properties: the vortex state vanishes as corners are eliminated, and the domain configuration changes with geometry. These results establish a simple and reproducible route for achieving different magnetic domain structures in 2D iron oxides and provide an experimental basis for simultaneous morphology-phase tailoring by tuning μ_O to attenuate in-plane magnetism.

Author contributions

Wenkai Liu: writing – original draft, methodology, investigation, formal analysis, and data curation. Huawei Zhao: methodology and formal analysis. Dongqi Zhao: formal analysis. Yupeng Zhao: writing – original draft and formal analysis. Muhammad Hamza Tariq: writing – review. Jinhong Du: writing – review. Ruotong Zhao: writing – review. Yanqing Ma: writing – review and editing, validation, supervision, and project administration. Lei Ma: writing – review and editing, supervision, methodology, and funding acquisition.

Conflicts of interest

There are no conflicts to declare.

Data availability

Details on data and materials are available in the article and its supplementary information (SI). Supplementary information: supplementary figures and additional computational details. See DOI: https://doi.org/10.1039/d5nr05160f.

Acknowledgements

This work was financially supported by the National Key R&D Program of China (No. 2022YFC3006303), the Tianjin Natural Science Foundation Project (No. 25JCZDJC01380) and the Innovation fund of Haihe Laboratory of Low-dimensional

Electronic Materials (25HHDWSS00005). The authors thank Dr Xin He for his discussion and suggestions for revision.

References

1 J. Mohapatra, A. Ramos, J. Elkins, J. Beatty, M. Xing, D. Singh, E. C. La Plante and J. Liu, *Appl. Phys. Lett.*, 2021, **118**, 183102.
2 H. Sun, M. Wang, W. Li, Y. Liu, X. Sun, W. Wang, Y. Guo, Y. Xie and C. Wu, *Sci. China: Chem.*, 2025, **68**, 1337–1344.
3 B. Zhang, P. Lu, R. Tabrizian, P. X. L. Feng and Y. Wu, *npj Spintron.*, 2024, **2**, 6.
4 Z. Zhao, Z. Fang, X. Han, S. Yang, C. Zhou, Y. Zeng, B. Zhang, W. Li, Z. Wang, Y. Zhang, J. Zhou, J. Zhou, Y. Ye, X. Hou, X. Zhao, S. Gao and Y. Hou, *Nat. Commun.*, 2023, **14**, 958.
5 Z. Jia, M. Zhao, Q. Chen, R. Sun, L. Cao, K. Ye, T. Zhu, L. Liu, Y. Tian, Y. Wang, J. Du, F. Zhang, W. Lv, F. Ling, Y. Zhai, Y. Jiang and Z. Wang, *Adv. Sci.*, 2024, **11**, 2405945.
6 W. Chu, R. Xin, L. Zou, X. Fan, X. Zhou, C. Li and Y. Zhou, *Phys. Status Solidi RRL*, 2024, **18**, 2300102.
7 Q. Wang, X. Zhang, S. Wang, Y. Wu, X. Wei, T. Han, F. Li, L. Shan and M. Long, *ACS Appl. Mater. Interfaces*, 2024, **16**, 60440–60447.
8 C. Yin, C. Gong, J. Chu, X. Wang, C. Yan, S. Qian, Y. Wang, G. Rao, H. Wang, Y. Liu, X. Wang, J. Wang, W. Hu, C. Li and J. Xiong, *Adv. Mater.*, 2020, **32**, 2002237.
9 T. Wang, Z. Fan, W. Xue, H. Yang, R.-W. Li and X. Xu, *Nano Lett.*, 2023, **23**, 10498–10504.
10 Z. Jia, W. Wang, Z. Li, R. Sun, S. Zhou, F. L. Deepak, C. Su, Y. Li and Z. Wang, *ACS Appl. Mater. Interfaces*, 2021, **13**, 24051–24061.
11 Z. Jia, Q. Chen, W. Wang, R. Sun, Z. Li, R. Hübner, S. Zhou, M. Cai, W. Lv, Z. Yu, F. Zhang, M. Zhao, S. Tian, L. Liu, Z. Zeng, Y. Jiang and Z. Wang, *Adv. Sci.*, 2024, **11**, 2401944.
12 L. Zhou, K. Xu, A. Zubair, X. Zhang, F. Ouyang, T. Palacios, M. S. Dresselhaus, Y. Li and J. Kong, *Adv. Funct. Mater.*, 2017, **27**, 1603491.
13 M. Zhu, H. Xu, Z. Tan and L. Wang, *Results Phys.*, 2023, **47**, 106321.
14 P. Bargiela, V. Fernandez, D. Morgan, N. Fairley and J. Baltrusaitis, *Surf. Interface Anal.*, 2024, **56**, 189–199.
15 P. Wang, J. Ge, J. Luo, H. Wang, L. Song, Z. Li, J. Yang, Y. Wang, R. Du, W. Feng, J. Wang, J. He and J. Shi, *Nano Lett.*, 2023, **23**, 1758–1766.
16 Y. Xiang, N. An, G. Zhang, L. Wang and X. Chen, *J. Nanoelectron. Optoelectron.*, 2024, **19**, 564–571.
17 M. Toda-Casaban, L. Balcells, N. Mestres, A. Pomar, H. Chen, A. G. Manjón, J. Arbiol, B. Martínez and C. Frontera, *Acta Mater.*, 2025, **301**, 121613.
18 J. Niu, Y. Jiang, Y. He, A. Tao, C. Chen, X.-L. Ma and H. Ye, *Comput. Mater. Sci.*, 2022, **210**, 111442.
19 T. Yamashita and P. Hayes, *Appl. Surf. Sci.*, 2008, **254**, 2441–2449.
20 P. Garg and U. Deshpande, *Braz. J. Phys.*, 2025, **55**, 81.
21 J. Yuan, A. Balk, H. Guo, Q. Fang, S. Patel, X. Zhao, T. Terlier, D. Natelson, S. Crooker and J. Lou, *Nano Lett.*, 2019, **19**, 3777–3781.
22 F.-X. Ma, X.-Y. Sun, K. He, J.-T. Jiang, L. Zhen and C.-Y. Xu, *J. Magn. Magn. Mater.*, 2014, **361**, 161–165.
23 C. Li, R. Wei, Y. Xu, A. Sun and L. Wei, *Nano Res.*, 2014, **7**, 536–543.
24 X. Huang, S. K. Ramadugu and S. E. Mason, *J. Phys. Chem. C*, 2016, **120**, 4919–4930.
25 X. Wei, Z. Ma, X. Mu, Q. Zhang and B. Hu, *Mol. Catal.*, 2021, **499**, 111303.
26 R. Yu. Rudenko and A. V. Chzhan, *J. Sib. Fed. Univ., Chem. – Math. Phys.*, 2015, **8**, 327–339.
27 A. Mandziak, J. E. Prieto, C. Gutiérrez-Cuesta, M. A. Niño, M. Foerster, J. de la Figuera and P. Nita, *Sci. Rep.*, 2025, **15**, 10549.
28 J. Zang, V. Cros and A. Hoffmann, *Topology in Magnetism*, Springer International Publishing, 2018.
29 W. Xue, T. Wang, H. Yang, H. Zhang, G. Dai, S. Zhang, R. Yang, Z. Quan, R.-W. Li, J. Tang, C. Song and X. Xu, *Nat. Commun.*, 2025, **16**, 440.
30 A. Tao, Y. Jiang, S. Chen, Y. Zhang, Y. Cao, T. Yao, C. Chen, H. Ye and X.-L. Ma, *Nat. Commun.*, 2024, **15**, 6099.